Remote detection of widespread indigenous water in lunar pyroclastic deposits

Ralph E. Milliken and Shuai Li*

Laboratory analyses of lunar samples provide a direct means to identify indigenous volatiles and have been used to argue for the presence of Earth-like water content in the lunar interior. Some volatile elements, however, have been interpreted as evidence for a bulk lunar mantle that is dry. Here we demonstrate that, for a number of lunar pyroclastic deposits, near-infrared reflectance spectra acquired by the Moon Mineralogy Mapper instrument onboard the Chandrayaan-1 orbiter exhibit absorptions consistent with enhanced OH- and/or H_2O-bearing materials. These enhancements suggest a widespread occurrence of water in pyroclastic materials sourced from the deep lunar interior, and thus an indigenous origin. Water abundances of up to 150 ppm are estimated for large pyroclastic deposits, with localized values of about 300 to 400 ppm at potential vent areas. Enhanced water content associated with lunar pyroclastic deposits and the large areal extent, widespread distribution and variable chemistry of these deposits on the lunar surface are consistent with significant water in the bulk lunar mantle. We therefore suggest that water-bearing volcanic glasses from Apollo landing sites are not anomalous, and volatile loss during pyroclastic eruptions may represent a significant pathway for the transport of water to the lunar surface.

Understanding the current distribution and hosts of water on the Moon is necessary to constrain volatile behaviour during the Moon-forming giant impact event, potential sources and mechanisms for volatile delivery during and after accretion, and the role of water in lunar magmatic processes. Near-infrared (NIR) reflectance spectra acquired by three different space-based spectrometers exhibit absorptions near a wavelength of ∼3 μm that are consistent with OH/H_2O (hereafter referred to as 'water') at the optical surface of the Moon[1–4], commonly believed to result from exogenous sources including solar wind interaction with the lunar regolith and impact delivery of volatiles[1–4]. In contrast, the lunar interior and bulk mantle has historically been regarded as volatile-poor. This notion has been strongly challenged over the past several years by mounting evidence for the presence of indigenous water in returned lunar samples, including water in lunar pyroclastic glasses, olivine-hosted melt inclusions, apatite grains and anorthosite[5–8]. However, using these measurements to constrain the volatile inventory and magmatic history of the Moon as a whole is complicated by uncertainties in magma degassing and cooling history, to name a few[6,9]. Petrologic models that track the evolution of a crystallizing lunar magma ocean suggest the bulk cumulate mantle may be relatively dry (<10 ppm H_2O)[10], and measurements of chlorine isotopes[11] and zinc[12] may also indicate a dry bulk mantle.

These apparently conflicting lines of evidence have been used to suggest that water-rich lunar samples may not be representative of the bulk Moon and that they instead reflect anomalous volatile-rich magma source regions[12]. The small number of locations that have been directly sampled is an inherent limitation in trying to resolve this question using returned lunar samples, but remote sensing methods provide an alternative means to identify and characterize deposits with potential indigenous water at a global scale. Moon Mineralogy Mapper (M^3) NIR reflectance spectra have been used to identify isolated occurrences of potential magmatic water for the central peak of Bullialdus crater[13] and non-mare volcanic terrains at Compton–Belkovich[14], but proper identification and interpretation of water absorptions in M^3 data are often hindered by the presence of thermally emitted radiation at wavelengths >2 μm (refs 2,4,15). A

new thermal correction model for M^3 data was recently developed[16], allowing for improved estimates of the spatial distribution of water at the optical surface of the Moon, including dark 'mantle' deposits commonly interpreted to represent pyroclastic materials[17–19]. All M^3 radiance data used in this study were reduced to surface reflectance spectra, and then single scattering albedo, using this new correction and previously reported methods (see Methods).

Quantifying water content with M^3 data

The effective single particle absorption thickness (ESPAT) of Hapke[20] is a parameter for quantifying absorption strength at a given wavelength (see Methods), and ESPAT values for each thermally corrected M^3 pixel were calculated at ∼2.85 μm and are presented in Fig. 1 for the latitude range $\pm35°$. It is clear that very few regions in this latitude range exhibit measurable water absorption features (ESPAT values >0) even after implementation of the new thermal correction, consistent with previous studies that demonstrated water content increases primarily as a function of latitude[1–4]. However, many previously recognized pyroclastic deposits[17–19] exhibit significantly higher ESPAT values than surrounding terrains (Figs 1–3), demonstrating these deposits host previously unrecognized water sourced from the lunar interior. This is observed for many different sizes of deposits, but here we focus on those classified as 'very large'[18] as they are the most volumetrically significant deposits.

A linear relationship between ESPAT and wt%H_2O was previously used to estimate water contents of the lunar surface from NIR spectra acquired by the Deep Impact spacecraft[3], and this trend was explored for this study using laboratory spectra of anorthosite, water-bearing terrestrial volcanic glasses and synthetic glasses of lunar composition. These new laboratory measurements and independent numerical simulations confirm that ESPAT values can be used as a linear proxy for water content and that the slope of the ESPAT-H_2O trend varies as a function of particle size (that is, optical path length) (see Methods and Supplementary Fig. 2). To estimate absolute water content we assume an average particle size of 60–80 μm for lunar regolith materials, values that are within the
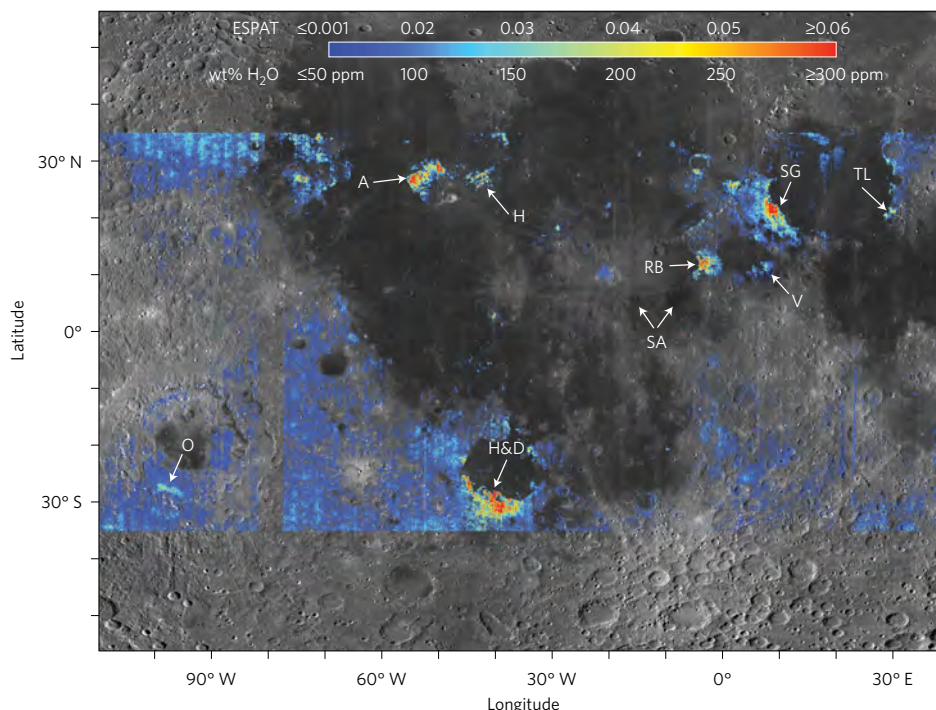
Department of Earth, Environmental, and Planetary Sciences, Brown University, Providence, Rhode Island 02912, USA. *e-mail: shuaili@hawaii.edu

Figure 1 | Map of ESPAT values at 2.85 μm and associated water contents derived from M³ spectra for ±35° latitude. Numerous locations of increased water content (arrows) are associated with previously recognized pyroclastic deposits ranging in area from thousands of square kilometres[18] to much smaller deposits recently identified in high-resolution Lunar Reconnaissance Orbiter Camera (LROC) images[19]. A, Aristarchus Plateau; H, Harbinger; H&D, Humorum & Doppelmayer; O, Orientale; RB, Rima Bode; SA, Sinus Aestuum; SG, Sulpicius Gallus; TL, Taurus–Littrow; V, Vaporum.

typical range of mean grain size measured for Apollo soil samples (45–100 μm)[21] (see Supplementary Information).

Enhanced water absorptions in pyroclastic deposits

A histogram of estimated water contents reveals that nearly all M³ pixels within the ±35° latitude zone are consistent with <100 ppm H_2O (Supplementary Fig. 2c) and the majority of pixels exhibit no strong evidence of water, regardless of soil maturity or whether they are associated with highland or mare compositions. These values overlap the range observed for lunar samples based on pyrolysis experiments at temperatures >300 °C (Supplementary Fig. 2c and Methods), and although such values may be affected by terrestrial contamination it is also recognized that lunar regolith grains contain measurable water resulting from solar wind implantation[22,23]. We adopt a water content of ~100 ppm as a conservative 'background' value attributable to solar wind implantation for lunar soils in the ±35° latitude range, a value that is broadly similar to the estimated ~70 ppm in Apollo soil 10084 based on measured water contents of its agglutinitic glass[22]. Locations with water contents and associated ESPAT values significantly above this level between ±35° latitude are considered to have excess water that is inconsistent with a purely solar wind origin.

None of the observed regions of excess water are clearly associated with impact craters or ejecta, ruling out an origin by impact delivery. The most spatially extensive areas of excess water are all associated with inferred pyroclastic deposits, including dark mantling deposits near the Apollo 15 and 17 landing sites (Figs 1,3 and 4 and Supplementary Figs 3 and 4). Potential grain size differences between pyroclastic deposits and typical lunar regolith cannot fully account for their apparent differences in ESPAT values or inferred water contents (see Supplementary Information). Glass-rich soils sampled at the Apollo 15 and 17 sites, for instance, have a smaller mean particle size than typical poorly sorted lunar regolith[21], whereas the opposite would need to be true for pyroclastic deposits to explain the observed differences. In addition, ESPAT values are

at or close to 0 for M³ spectra of highland and mare soils at these latitudes, and indicate water is not present regardless of particle size, including for terrains directly adjacent to pyroclastic deposits that by contrast exhibit clear absorption features (Fig. 3).

Water abundance and implications for the lunar interior

Estimated bulk water contents vary within and between large pyroclastic deposits, but most M³ pixels are consistent with ≤150 ppm after accounting for 100 ppm of potential solar wind implantation (Fig. 4 and Supplementary Fig. 5). However, several pyroclastic deposits exhibit localized enrichments of up to ~300–400 ppm after background subtraction (Supplementary Fig. 5), and deposits with greater areal extent exhibit higher mean water contents (Fig. 4). Although numerous eruption events and vents may contribute to a single dark mantle deposit, this observation is broadly consistent with magma ascent and eruption models that predict eruption extent to scale with volatile content[24]. Our results also suggest pyroclastic deposits inferred to have higher titanium content exhibit higher average water contents compared with lower-Ti deposits of similar areal extent (Fig. 4d). This trend is consistent with experiments that indicate faster cooling rates (and thus less degassing) for high-Ti orange glass beads[25,26], but it may also indicate a difference in volatile content of the magma source regions. These possibilities cannot be distinguished solely on the basis of remote sensing methods, but the apparent difference in water content between high- and low-Ti pyroclastic deposits raises tantalizing possibilities about large-scale heterogeneity in the volatile content of the deep mantle or fundamental links between magma composition and physical eruption processes on the Moon. We also observe that excess water contents are lower and more spatially restricted at the Sinus Aestuum pyroclastic deposit relative to its mapped extent when compared with other large pyroclastic deposits (Supplementary Fig. 6). Sinus Aestuum is also the only large dark mantle deposit to exhibit numerous occurrences of spinel[27,28], a possible indicator that this deposit
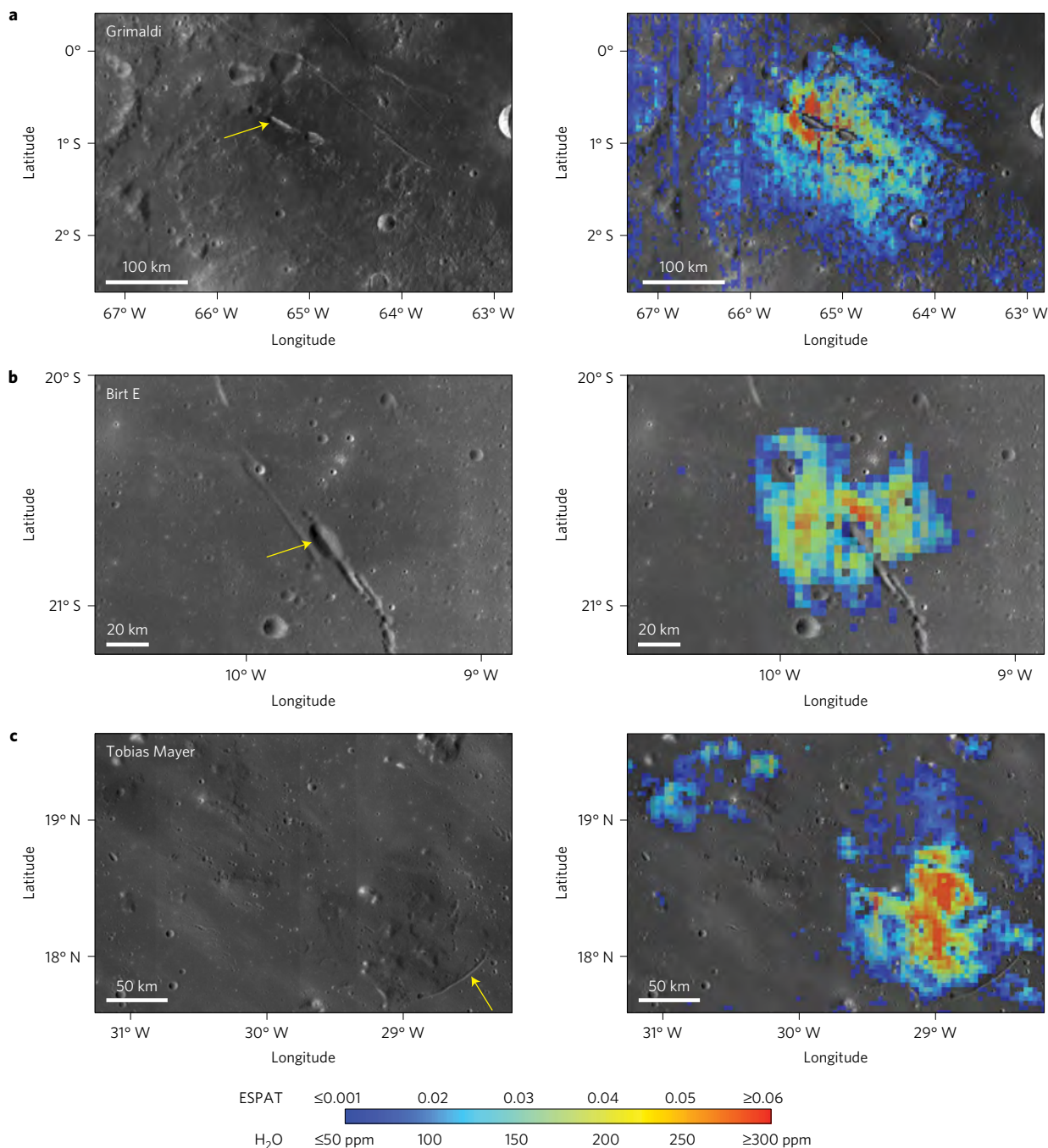
Figure 2 | Visible images and water contents for select small dark mantle deposits. a–c, Images in the left column are from LRO wide-angle camera (WAC) mosaic and highlight potential vents/fissures (yellow arrows); the right column shows ESPAT/H$_2$O maps overlain on WAC images. Deposits at Grimaldi[18] (**a**) and recently identified pyroclastic candidates at Birt E[19] (**b**) and Tobias Mayer[19] (**c**).

may record a magmatic history that is distinct from other large pyroclastic deposits[29].

Water contents measured in lunar glass beads (<50 ppm) have been used in conjunction with degassing models to infer pre-eruptive water contents of 260–745 ppm, and measured water contents of olivine-hosted melt inclusions in lunar volcanic glass range from 615 to 1,410 ppm (yielding pre-eruptive contents of ∼485–1,114 ppm after accounting for post-entrapment crystallization)[5,6]. Based on these values, and under the assumptions outlined here, our commonly observed water contents of <150 ppm would imply moderate to significant degassing has occurred for most lunar pyroclastic deposits. However, our highest estimated water contents are closer to the potential pre-eruptive water contents

stated above. At some locations the regions with the strongest absorptions and highest inferred water contents are adjacent to fissures and potential vents (Fig. 2), areas where expanding vapour clouds may have been densest. Alternatively, observed increases in water content towards vents may reflect overestimation due to a relative increase in the average particle size of beads towards the eruption source, a factor that is not accounted for in the current analysis but that may be expected for pyroclastic deposits.

Despite the complexities of extracting quantitative information from surface reflectance spectra, the observation of enhanced water absorptions in lunar pyroclastic deposits relative to typical lunar soils indicates the presence of indigenous magmatic volatiles in these locations. Although not all pyroclastic deposits exhibit
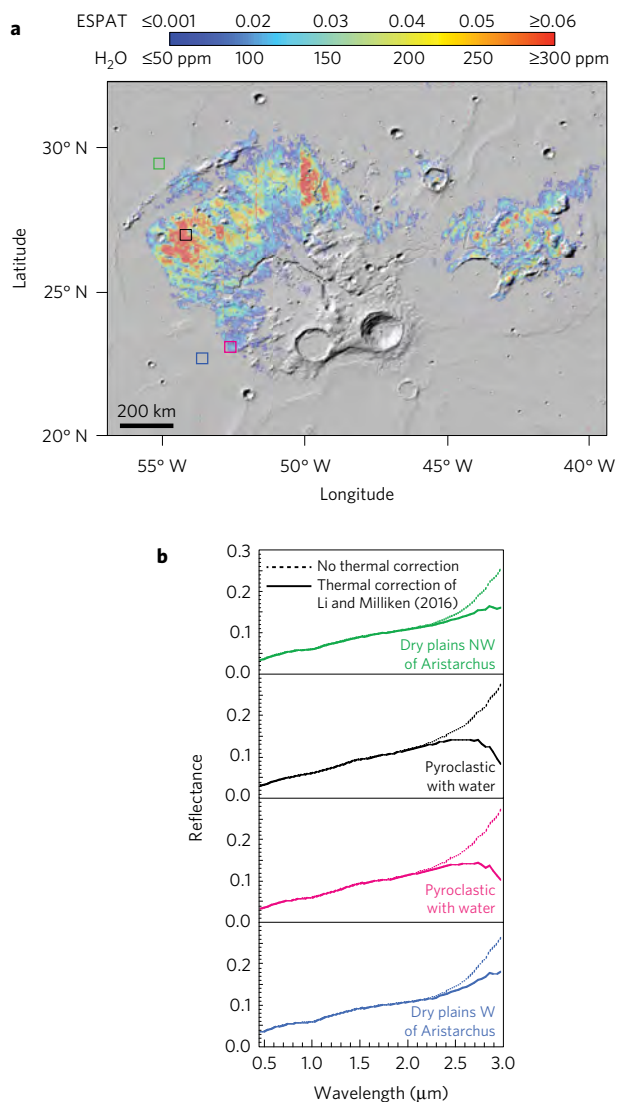
Figure 3 | Results for Aristarchus region. a, Water content map. **b**, Example pre- and post-thermal correction M³ reflectance spectra for dark mantle deposits (black and magenta spectra) and surrounding terrains (green and blue spectra); spectra correspond to coloured boxes in **a**. A clear increase in OH/H₂O absorption strength is observed at the longest wavelengths (≥2.7 μm) for the pyroclastic deposit.

a significant enhancement, the widespread occurrence of water in pyroclastic deposits of likely different compositions supports the presence of volumetrically significant, water-bearing magma source regions within the lunar interior. These results demonstrate that water-bearing glasses in returned lunar samples are not local anomalies, and the nearly ubiquitous presence of water in large and small lunar pyroclastic deposits adds to the growing evidence that the lunar mantle is an important reservoir of water. Further study is warranted to improve quantitative estimates of H₂O content from M³ and similar NIR reflectance data, but the data presented here indicate pyroclastic eruptions played an important role in transferring water from the deep interior to the lunar surface. Large pyroclastic deposits may thus be a viable source of water for *in situ* resource utilization during future lunar surface exploration.

Methods

Methods, including statements of data availability and any associated accession codes and references, are available in the online version of this paper.

References

1. Clark, R. N. Detection of adsorbed water and hydroxyl on the Moon. *Science* **326,** 562–564 (2009).
2. Pieters, C. M. Character and spatial distribution of OH/H₂O on the surface of the Moon seen by M³ on Chandrayaan-1. *Science* **326,** 568–572 (2009).
3. Sunshine, J. *et al*. Temporal and spatial variability of lunar hydration as observed by the Deep Impact spacecraft. *Science* **326,** 565–568 (2009).
4. McCord, T. B. *et al*. Sources and physical processes responsible for OH/H₂O in the lunar soil as revealed by the Moon Mineralogy Mapper (M³). *J. Geophys. Res.* **116,** E00G05 (2011).
5. Saal, A. *et al*. Volatile content of lunar volcanic glasses and the presence of water in the Moon's interior. *Nature* **454,** 192–195 (2008).
6. Hauri, E. H., Saal, A. E., Rutherford, M. J. & Van Orman, J. A. Water in the Moon's interior: truth and consequences. *Earth Planet. Sci. Lett.* **409,** 252–264 (2015).
7. Robinson, K. L. & Taylor, G. J. Heterogeneous distribution of water in the Moon. *Nat. Geosci.* **7,** 401–408 (2014).
8. Chen, Y. *et al*. Water, fluorine, and sulfur concentrations in the lunar mantle. *Earth Planet. Sci. Lett.* **427,** 37–46 (2015).
9. Sharp, Z. D., McCubbin, F. M. & Shearer, C. K. A hydrogen-based oxidation mechanism relevant to planetary formation. *Earth Planet. Sci. Lett.* **380,** 88–97 (2013).
10. Elkins-Tanton, L. T. & Grove, T. L. Water (hydrogen) in the lunar mantle: results from petrology and magma ocean modeling. *Earth Planet. Sci. Lett.* **307,** 173–179 (2011).
11. Sharp, Z. D., Shearer, C. K., McKeegan, K. D., Barnes, J. D. & Wang, Y. Q. The chlorine isotope composition of the Moon and implications for an anhydrous mantle. *Science* **329,** 1050–1053 (2010).
12. Albarède, F., Albalat, E. & Lee, C.-T. A. An intrinsic volatility scale relevant to the Earth and Moon and the status of water in the Moon. *Meteorol. Planet. Sci.* **50,** 568–577 (2015).
13. Klima, R., Cahill, J., Hagerty, J. & Lawrence, D. Remote detection of magmatic water in Bullialdus Crater on the Moon. *Nat. Geosci.* **6,** 737–741 (2013).
14. Bhattacharya, S. *et al*. Endogenic water on the Moon associated with nonmare silicic volcanism: implications for hydrated lunar interior. *Curr. Sci.* **105,** 685–691 (2013).
15. Clark, R. N., Pieters, C. M., Green, R. O., Boardman, J. W. & Petro, N. E. Thermal removal from near-infrared imaging spectroscopy data of the Moon. *J. Geophys. Res.* **116,** E00G16 (2011).
16. Li, S. & Milliken, R. E. An empirical thermal correction model for Moon Mineralogy Mapper data constrained by laboratory spectra and Diviner temperatures. *J. Geophys. Res.* **121,** 2081–2107 (2016).
17. Weitz, C. M., Head, J. W. III & Pieters, C. Lunar regional dark mantle deposits: geologic, multispectral, and modeling studies. *J. Geophys. Res.* **103,** 22725–22759 (1998).
18. Gaddis, L. R., Staid, M. I., Tyburczy, J. A., Hawke, B. R. & Petro, N. E. Compositional analyses of lunar pyroclastic deposits. *Icarus* **161,** 262–280 (2003).
19. Gustafson, J. O., Bell, J. F., Gaddis, L. R., Hawke, B. R. & Giguere, T. A. Characterization of previously unidentified lunar pyroclastic deposits using Lunar Reconnaissance Orbiter Camera data. *J. Geophys. Res.* **117,** E00H25 (2012).
20. Hapke, B. *Theory of Reflectance and Emittance Spectroscopy* (Cambridge Univ. Press, 1993).
21. McKay, D. S., Heiken, G., Basu, A., Blanford, G. & Simon, S. in *Lunar Sourcebook: A User's Guide to the Moon* (eds Heiken, G. H., Vaniman, D. T. & French, B. M.) 283–356 (1991).
22. Liu, Y. *et al*. Direct measurement of hydroxyl in the lunar regolith and the origin of lunar surface water. *Nat. Geosci.* **5,** 779–782 (2012).
23. Stephant, A. & Robert, F. The negligible chondritic contribution in the lunar soils water. *Proc. Natl Acad. Sci. USA* **111,** 15007–15012 (2014).
24. Wilson, L. & Head, J. W. III Ascent and eruption of basaltic magma on the Earth and Moon. *J. Geophys. Res.* **86,** 2971–3001 (1981).
25. Arndt, J. & Engelhardt, W. Formation of Apollo 17 orange and black glass beads. *J. Geophys. Res.* **92,** E372–E376 (1987).
26. Arndt, J. & Engelhardt, W. V. Formation of Apollo 15 green glass beads. *J. Geophys. Res.* **89,** C225–C232 (1984).
27. Sunshine, J. M., Petro, N. E., Besse, S. & Gaddis, L. Widespread exposures of small scale spinel-rich pyroclastic deposits in Sinus Aestuum. In *Proc. 45th Lunar Planet. Sci. Conf.* 2297 (2014); https://www.hou.usra.edu/meetings/lpsc2014/pdf/2297.pdf
28. Yamamoto, S. *et al*. A new type of pyroclastic deposit on the Moon containing Fe-spinel and chromite. *Geophys. Res. Lett.* **40,** 4549–4554 (2013).
29. Williams, K. B. *et al*. Reflectance spectroscopy of chromium-bearing spinel with application to recent orbital data from the Moon. *Am. Mineral.* **101,** 726–734 (2016).
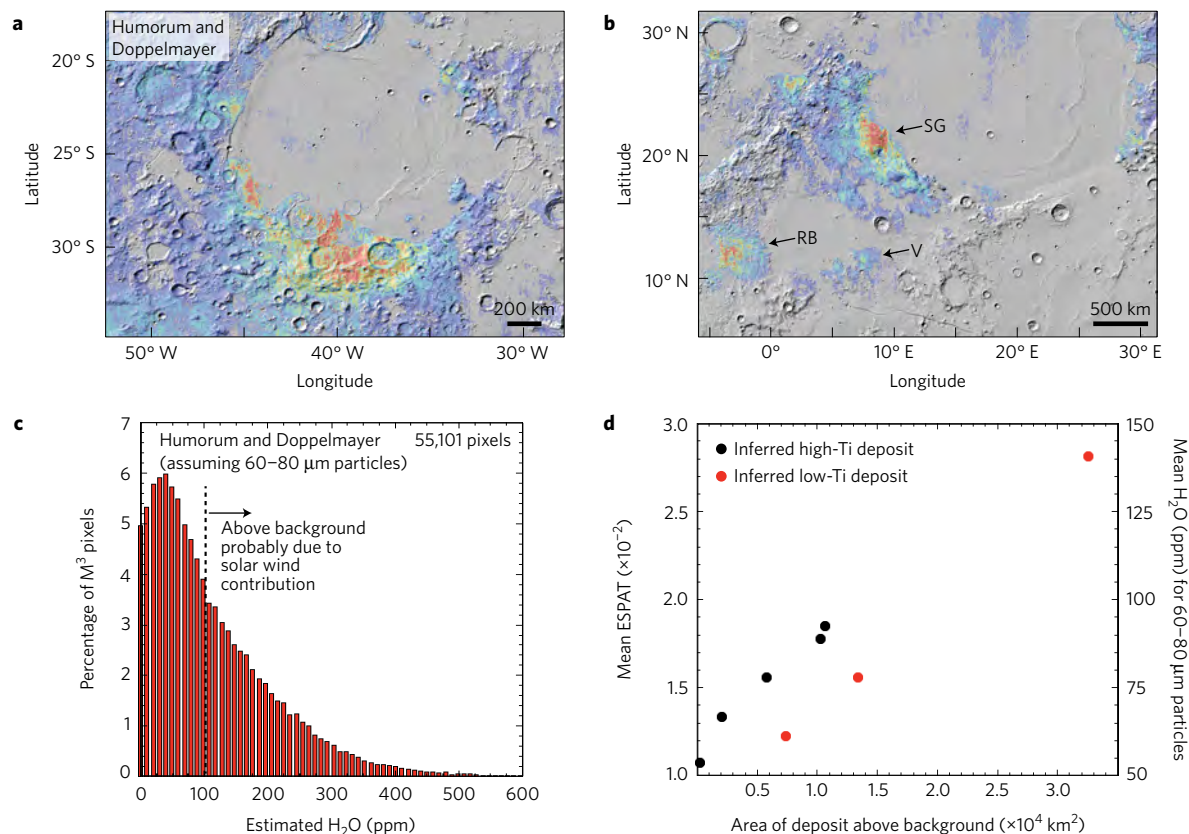
Figure 4 | Estimated water contents for select large pyroclastic deposits. a,b, Water content maps for Humorum and Doppelmayer (**a**), and Sulpicius Gallus (SG), Rima Bode (RB) and Vaporum (V) (**b**). Colours represent the same values as in Fig. 3. **c**, Example histogram for data shown in **a** demonstrating numerous regions are above the background value; pixels with value of zero are not included in histogram. **d**, Plot of average ESPAT/water content versus areal extent; areas are determined by number of M^3 pixels above the ~100 ppm background. Relative titanium contents are from the classification of Gaddis and colleagues[18].

Author contributions

R.E.M. wrote the manuscript, interpreted the data and contributed to data analysis. S.L. processed M^3 data, made lab measurements and simulations, and contributed to data interpretation. S.L. initiated the draft for the Methods.

Additional information

Supplementary information is available in the online version of the paper. Reprints and permissions information is available online at www.nature.com/reprints. Publisher's note: Springer Nature remains neutral with regard to jurisdictional claims in published maps and institutional affiliations. Correspondence and requests for materials should be addressed to S.L.

Competing financial interests

The authors declare no competing financial interests.

Methods

Conversion of M³ data to reflectance. M³ radiance data were processed to reflectance using the same methods employed by the M³ team[30,31], with the exception of the thermal correction as described below. The reader is referred to Li and Milliken[16] for a detailed description of these methods, but a brief overview is provided here. We rely on the solar spectrum provided in the Planetary Data System (PDS) dataset to convert radiance at sensor to apparent reflectance (I/F) and use the geometry information provided for each image cube to account for photometric effects and viewing geometry. The Lommel–Seeliger model is used for M³ photometric correction following the same approach that was done for Clementine spectral data[32–34]. M³ reflectance data are normalized to a 'standard' viewing geometry at $i = 30°$, $e = 0°$, and $g = 30°$. These corrections allow for direct comparison Level 2 M³ reflectance spectra that are available in the PDS. An exception is that we do not use the 'statistical polish' in our processing pipeline, which may lead to minor differences between our calculated reflectance spectra and those available through the PDS[16]. These small differences do not affect the results or interpretations of the work presented here.

Thermal correction of M³ data. The thermal correction model for M³ data used in this study is described in detail in Li and Milliken[16]. It has been suggested in previous studies[11] that thermal removal method of Clark *et al.*[15] used for the publicly available M³ Level 2 data (reflectance spectra) may be insufficient for evaluating lunar surface water in regions where radiance at sensor includes a thermal contribution from the lunar surface. A new semi-empirical thermal correction model for M³ data was recently developed based on laboratory reflectance spectra of Apollo samples, and this model has been independently validated with a radiative transfer model in conjunction with lunar surface temperatures measured by the Diviner instrument on the Lunar Reconnaissance Orbiter[16]. Laboratory reflectance spectra of Apollo samples measured under ambient conditions were collated, and Li and Milliken[16] proposed an empirical model based on the correlation between reflectance values at 1.55 μm (band 49 of M³ images) and at 2.54 μm (band 74 of M³ images).

A short wavelength of 1.55 μm was selected because there are no major absorptions near this region for lunar materials and it is not affected by thermal emission even at maximum lunar surface temperatures. A long wavelength of 2.54 μm was selected because it is far enough beyond pyroxene absorption centred at ~2 μm, lies outside of the OH stretching band centred at ~2.8–2.9 μm, and can be affected by thermal emission under a wide range of lunar surface temperatures. The reflectance at 1.55 μm is highly correlated to the reflectance at 2.54 μm in lab reflectance spectra of Apollo and Luna samples (where there are no thermal emission effects), thus the former can be used to predict the latter within ~2% absolute reflectance for a wide range of lunar materials.

Diviner-based surface temperature data for several regions of interest (covering a wide variety of optical maturity, albedo, solar incidence angle, latitude and composition) were used to estimate and remove thermal contributions from M³ data acquired at the same locations at the same lunar local time. Important for the current study, independently measured Diviner-based temperatures were evaluated at several locations with pyroclastic deposits, including Aristarchus, Humorum and Aestuum, and it was confirmed that the final empirical thermal correction is applicable to M³ data of dark mantle deposits[16]. A Hapke-based radiative transfer model[20] was applied to the M³ data using the matched Diviner surface temperatures, which yielded thermally corrected reflectance spectra for each M³ pixel within the regions of interest. The correlation between reflectance at 1.55 and 2.54 μm in these thermally corrected M³ data was effectively the same as the trend observed in lab spectra of the Apollo samples, indicating it is an inherent property in reflectance spectra of materials that typify the lunar surface, including for the evaluated dark mantle deposits.

Based on these results, it was concluded that the previously used thermal correction model[15] commonly underestimated surface temperatures by 10–20 K or more. It was also concluded that reflectance values observed at 1.55 μm in M³ data could be used to predict the reflectance values at 2.54 μm, and any excess reflectance at the longer wavelengths can be assumed to result from thermal emission[16]. Any excess thermal emission can then be estimated and removed from the original radiance data prior to conversion to surface reflectance. A key benefit of this model is that M³ data can be thermally corrected without the need for independently measured surface temperatures acquired at the same local lunar time of day. The thermally corrected spectra have an uncertainty of ±2% or better absolute reflectance at wavelengths affected by thermal emission.

Conversion of M³ reflectance data to single scattering albedo & derivation of ESPAT. Thermally corrected M³ reflectance spectra are converted to single scattering albedo (SSA) using the model of Hapke[20] (for example, equation 1 below) and adopting the parameterization of Li and Li[35]. The SSA spectra are then continuum-removed to account for the spectral slope over the ~3 μm region, and the resulting spectra are used to calculate the ESPAT values for each spectrum (M³ pixel) at a specified wavelength based on the procedures described below. For this

study, we used M³ band 82 (~2.85 μm) to calculate the ESPAT value to avoid the edge of the detector (band 85) and because it is close to the typical absorption maximum (~2.8–2.9 μm) for OH/H₂O-bearing materials. Analysis of laboratory reflectance spectra of Apollo samples used in the study of Li and Milliken[16] shows that the conversion from reflectance to SSA removes most of the spectral slope over the ~2.5–4 μm wavelength range. Therefore, the value of the continuum slope at 2.85 μm is projected to be similar to the SSA value observed at 2.54 μm (that is, the continuum slope over the ~3 μm region is very close to a horizontal line after converting to SSA).

These procedures are carried out for each M³ spectral image cube. Individual image cubes are then map-projected using the associated geometrical information, where we adopt a simple cylindrical map projection. Individual images are then mosaicked to produce a global map of M³ ESPAT values at ~2.85 μm at a scale of 1 km pixel⁻¹. M³ image cubes from all optical periods were examined to create the best coverage global map.

Radiance measured by M³ (and thus derived ESPAT values) may vary for a given location for data acquired during different optical periods. Although this may lead to differences in scale and/or range in ESPAT values when comparing data between different optical periods, we note that the pyroclastics consistently exhibit higher ESPAT values compared with surrounding terrains for data acquired within a given optical period. In addition, the trends associated with pyroclastic deposits are observed in the different optical periods when overlapping data exist, indicating enhancements in pyroclastics are not the result of anomalous instrument behaviour associated with a given optical period. For the aggregate ESPAT map shown in Fig. 1 we use data from optical period OP2C whenever possible, because it provides the greatest coverage, and gaps are filled in by data from OP1B. Nearly all large pyroclastic deposits are covered by data from OP2C, although portions of Rima Bode, Humorum and Doppelmayer are incomplete and are covered by data from OP1B. This may lead to differences in reported absolute water content for these locations compared with what may have been observed if coverage existed for OP2C. ESPAT maps for the individual optical periods are presented in Supplementary Fig. 1.

Uncertainties in ESPAT and water content values derived from M³ data. Uncertainties in ESPAT values resulting from the potential 2% uncertainty associated with the thermal correction were also evaluated. ESPAT values for each pixel in the regions of interest studied by Li and Milliken[16], which included regions associated with dark mantle deposits, were calculated based on M³ spectra that were thermally corrected using the Diviner surface temperatures. These values were then compared with ESPAT values derived from M³ data that were thermally corrected using the final empirical approach, which may lead to ±2% uncertainty in reflectance. Results of this comparison show that ESPAT values calculated from thermally corrected spectra based on the empirical method may differ by 20% (relative) compared with ESPAT values determined from spectra corrected using actual Diviner-based temperatures. Because conversion of ESPAT to %H₂O is a simple scalar (the value of which is particle-size dependent), the relative uncertainty in estimated water content that is associated with potential uncertainty in ESPAT values propagated from uncertainty in the thermal correction is also 20%.

Determination of water content from reflectance spectra. Fundamental OH and H₂O absorptions observed in M³ data near ~3 μm can be used to estimate the absolute water content of lunar surface materials. Previous laboratory studies have shown that Hapke's effective single particle absorption thickness (ESPAT) parameter is linearly related to water content when derived at a wavelength of ~2.9 μm (refs 36–39). Unlike traditional band depth or apparent absorbance values based on reflectance spectra, the ESPAT parameter is expected to be a more accurate predictor of the abundance of an absorbing species because it is linearly proportional to a wider range of $\alpha \langle D \rangle$ values, where α is the absorption coefficient and $\langle D \rangle$ is the optical path length (related to particle size) of an absorbing component[20]. This has been confirmed for a variety of water-bearing minerals, where previous studies have shown that ESPAT values are linearly correlated to water content for a wide range of hydrated phases when calculated at ~2.9 μm, and the slope of the ESPAT-wt%H₂O trend was demonstrated to be largely invariant with composition for a number of hydrated minerals[36–39].

This method has been previously used to quantify the water content of the martian surface[40,41] as well as the lunar surface[3] using reflectance spectra acquired by the Mars Express OMEGA instrument and Deep Impact mission, respectively. However, both laboratory experiments and numerical simulations show that the slope of the ESPAT-wt%H₂O trend is dependent on particle size[39,42]. The ESPAT-wt%H₂O trend was further explored by Li[43] for lunar-relevant materials, including hydrated volcanic glasses (terrestrial samples of mid-ocean ridge basalt and synthetic glasses of lunar composition) and a sample of terrestrial anorthosite (Supplementary Fig. 2). An overview of the methods and results of Li[43] is provided below, but for detailed descriptions and example spectra of samples the reader is referred to that work.

Laboratory samples. A sample of terrestrial anorthosite from Timmins, Ontario, provided by R. Milliken (Brown University), was ground and sieved to <45 μm. Sample weight and reflectance spectra (~1 μm–25 μm) were recorded at ambient temperature, after 20 min of purging in dry air, and after heating from 100 to 600 °C in 50 °C increments for 30 min at each step. Sample weight and spectra were measured immediately after each heating step to avoid contamination from atmospheric water. Weight loss was assumed to be due to water loss for each heating step.

A suite of mid-ocean ridge basalt (MORB) glasses were provided by A. Saal (Brown University) to explore volcanic samples with a wider range in water content than present in the synthetic lunar glasses, and also to assess variations as a function of particle size. Two criteria were used for selection of these samples. First, the water content should be less than 20,000 ppm (2 wt%), which is an appropriate range for lunar materials. Second, the samples should be as visually homogeneous and free of alteration as possible. Four samples in total were examined, and absolute water content of these glasses were previously measured by SIMS[44]. The sample information and their water contents are listed in Supplementary Table 1. These samples were sieved into four particle size ranges (<45 μm, 32–53 μm, 63–75 μm, and 106–125 μm) to determine how H_2O%-ESPAT trends may be affected by particle size and for comparison to the numerical ESPAT simulations described below. Stepwise heating experiments similar to what was done for the anorthosite were carried out.

Synthetic yellow and orange glasses of the same bulk chemical composition as the Apollo yellow and orange glasses were also measured to examine their H_2O%-ESPAT trend (Supplementary Fig. 2). These samples were synthesized under lunar-like conditions and characterized, including water contents via SIMS measurements (Supplementary Table 2), by Wetzel[45]. Samples were ground and dry-sieved to <45 μm diameter. RELAB FTIR spectra of these samples are presented in Supplementary Fig. 2d.

Acquisition and processing of lab reflectance spectra. Reflectance spectra for each sample were measured in the NASA Reflectance Experiment LABoratory (RELAB) facility at Brown University using a Nicolet FTIR over a wavelength range of ~1–25 μm. As described above, different particle size ranges and water contents were examined to determine relevant H_2O%-ESPAT trends. All reflectance spectra were converted to single scattering albedo (SSA spectra, ω) using the Hapke radiative transfer equation[20]:

$$R = \frac{\omega}{4\pi} \frac{\mu_0}{\mu_0 + \mu} \{[1 + B(g)]P(g) + H(\mu_0, \omega_{ave})H(\mu, \omega_{ave}) - 1\} \quad (1)$$

where μ_0 is the cosine of the incidence angle (i), μ is the cosine of the emergence angle (e), g is the phase angle, B(g) is the back scattering function, P(g) is the phase function, and the H functions account for multiple scattering processes.

The parameterization for this model is the same as that used in previous studies[16,35]. The resulting SSA spectra were then used in equation (5) to determine ESPAT values for the water absorptions at a wavelength of ~2.85 μm, which corresponds to the common maximum absorption position for hydrous materials:

$$ESPAT = \frac{\omega}{1 - \omega} \quad (2)$$

Numerical simulation of spectra and ESPAT-wt%H_2O trends. The ESPAT-wt%H_2O trend can also be numerically simulated using equations (1) and (2) and if the optical constants (real (n) and imaginary (k) components of the complex index of refraction) are known. This is because the single scattering albedo is a function of n, k, and the optical path length $\langle D \rangle$ (which can be related to particle size, d). This is defined as[20]:

$$\omega = S_e + (1 - S_e)\frac{(1 - S_i)\Theta}{1 - S_i\Theta} \quad (3)$$

where S_e is the external scattering coefficient and S_i is the internal scattering coefficient, defined by:

$$S_e = \frac{(n-1)^2 + k^2}{(n+1)^2 + k^2} + 0.05, \quad S_i = 1 - \frac{4}{n(n+1)^2} \quad (4)$$

and a simple form of the internal transmission factor, Θ, can be defined as:

$$\Theta = e^{-\alpha\langle D \rangle} \quad (5)$$

Using Hapke theory, the optical constants can thus be used to forward calculate ω and ESPAT for a given particle size.

A relationship between water concentration (c) and absorbance (A) at ~2.85 μm for a variety of silicate glasses was derived by Stolper[46], where these properties were related by:

$$c = \frac{18.02A}{d\rho\varepsilon} \quad (6)$$

where d, ρ, and ε are the thickness, density, and extinction coefficient of silicate glasses, respectively. In this work we adopted the average value of $\varepsilon = 67\,l\,mol^{-1}\,cm^{-1}$ reported by Stolper[46] for a variety of glass compositions (both silicic and basaltic). In radiative transfer theory:

$$A = \alpha\langle D \rangle \quad (7)$$

where α is the absorption coefficient, defined as:

$$\alpha = \frac{4\pi k}{\lambda} \quad (8)$$

and $\langle D \rangle$ is the optical path length. The optical path length can be related to particle diameter, d, by $\langle D \rangle = 0.2d$ for irregular shaped particles[47–49]. If we assume the density (ρ) of silicate glass to be $3\,g\,cm^{-3}$, and substitute A with $\alpha\langle D \rangle$, equation (8) can be rewritten as:

$$\alpha = (558.66 \pm 10\%)c \quad (9)$$

which can then be substituted into equation (4) for a given particle size (optical path length).

Here we assume n = 1.5 (an average between values for water (1.33) and silicate glasses (~1.7)); the term k in s_e is negligible because of its significantly smaller value compared with n for silicate minerals (k varies from 10^{-4} to 5×10^{-3} for silicate minerals)[35]. Particle size (d) is examined for several values, thus ω (and by extension, ESPAT) is a function only of α and d. Based on the above equations, ESPAT values can thus be modelled as a function of water content (H_2O%, c) and particle size (d) at a given wavelength (λ). Following these steps, ESPAT-wt%H_2O trends were numerically simulated for water-bearing glass (assuming the extinction coefficient of $67\,l\,mol^{-1}\,cm^{-1}$) for <45 μm, 32–53 μm, 63–75 μm, and 106–125 μm diameter particles.

The results are presented in Supplementary Fig. 2 for direct comparison with the lab measurements, where dashed lines are calculated using the mean particle size for each of the four scenarios. It is observed that smaller particles exhibit steeper ESPAT-wt%H_2O trends. In addition, the three sample types (anorthosite, synthetic lunar glasses, MORB glasses) all follow a similar ESPAT-wt%H_2O trend for the <45 μm particle size (Supplementary Fig. 2b).

Although the specific samples (glasses and otherwise) measured in this study are compositionally distinct from the ones measured in Stolper[46], this modelling step provides a first-order independent assessment of potential ESPAT-wt%H_2O trends as a function of particle size for comparison with the experimental results. Together, these observations suggest ESPAT-wt%H_2O trends are linear for the examined range of water content, linear for lunar-relevant compositions, and similar in slope for different compositions. These results are in agreement with previous studies where similar trends were observed for a wide variety of other hydrated phases[36–39]. Based on these results, ESPAT values derived from M^3 data are expected to be an appropriate linear proxy for water content[43].

Data availability. All original Moon Mineralogy Mapper (M^3) radiance data used for this work were downloaded from the NASA Planetary Data System (PDS) Geosciences node and are available at: http://geo.pds.nasa.gov/missions/chandrayaan1/default.htm. Other data acquired and used to support the findings of this study are available from the corresponding author upon request.

References

30. Green, R. O. et al. The Moon Mineralogy Mapper (M^3) imaging spectrometer for lunar science: instrument description, calibration, on-orbit measurements, science data calibration and on-orbit validation. *J. Geophys. Res.* **116,** E00G19 (2011).
31. Boardman, J. W. et al. Measuring moonlight: an overview of the spatial properties, lunar coverage, selenolocation, and related Level 1B products of the Moon Mineralogy Mapper. *J. Geophys. Res.* **116,** E00G14 (2011).
32. Hillier, J. K., Buratti, B. J. & Hill, K. Multispectral photometry of the Moon and absolute calibration of the Clementine UV/Vis camera. *Icarus* **141,** 205–225 (1999).
33. Buratti, B. J. et al. A wavelength-dependent visible and infrared spectrophotometric function for the Moon based on ROLO data. *J. Geophys. Res.* **116,** E00G03 (2011).
34. Lundeen, S., McLaughlin, S. & Alanis, R. Moon Mineralogy Mapper data product software interface specification. *Jet Propul. Lab.* **v9.10,** JPL D-39032 (2011).
35. Li, S. & Li, L. Radiative transfer modeling for quantifying lunar surface minerals, particle size, and submicroscopic metallic Fe. *J. Geophys. Res.* **116,** E09001 (2011).
36. Milliken, R. E. & Mustard, J. F. Quantifying absolute water content of minerals using near-infrared reflectance spectroscopy. *J. Geophys. Res.* **110,** E12001 (2005).

37. Milliken, R. E. *Estimating the Water Content of Geologic Materials Using Near-Infrared Reflectance Spectroscopy: Applications to Laboratory and Spacecraft Data* PhD thesis, Brown Univ. (2006).

38. Milliken, R. E. & Mustard, J. Estimating the water content of hydrated minerals using reflectance spectroscopy I. Effects of darkening agents and low-albedo materials. *Icarus* **189,** 550–573 (2007).

39. Milliken, R. E. & Mustard, J. Estimating the water content of hydrated minerals using reflectance spectroscopy II. Effects of particle size. *Icarus* **189,** 574–588 (2007).

40. Milliken, R. E. *et al*. Hydration state of the Martian surface as seen by Mars Express OMEGA: 2. H_2O content of the surface. *J. Geophys. Res.* **112,** E08S07 (2007).

41. Audouard, J. *et al*. Water in the Martian regolith from OMEGA/Mars Express. *J. Geophys. Res.* **119,** 1969–1989 (2014).

42. Pommerol, A. & Schmitt, B. Strength of the H_2O near-infrared absorption bands in hydrated minerals: effects of particle size and correlation with albedo. *J. Geophys. Res.* **113,** E10009 (2008).

43. Li, S. *Water on the Lunar Surface as Seen by the Moon Mineralogy Mapper: Distribution, Abundance, and Origins* PhD thesis, Brown Univ. (2016).

44. Shimizu, K. *et al*. Two-component mantle melting-mixing model for the generation of mid-ocean ridge basalts: implications for the volatile content of the Pacific upper mantle. *Geochim. Cosmochim. Acta* **176,** 44–80 (2016).

45. Wetzel, D. T. *Abundance, Speciation, and Role of Volatiles in Planetary Basalts* PhD thesis, Brown Univ. (2014).

46. Stolper, E. Water in silicate glasses: an infrared spectroscopic study. *Contrib. Mineral. Petrol.* **81,** 1–17 (1982).

47. Shkuratov, Y. G. Interpreting photometry of regolith-like surface with different topographies: shadowing and multiple scattering. *Icarus* **173,** 3–15 (2005).

48. Shkuratov, Y., Starukhina, L., Hoffmann, H. & Arnold, G. A model of spectral albedo of particulate surfaces: implications for optical properties of the Moon. *Icarus* **137,** 235–246 (1999).

49. Hapke, B. Bidirectional reflectance spectroscopy: 1. Theory. *J. Geophys. Res.* **86,** 3039–3054 (1981).